Received: 7 August 2025 | Revised: 13 October 2025 | Accepted: 20 November 2025 | Published online: 11 December 2025

RESEARCH ARTICLE

Journal of Optics and Photonics Research
2025, Vol. 00(00) 1–10
DOI: 10.47852/bonviewJOPR52027104

First-Principles Study of the Structural, Electronic, and Optical Properties of $NaTaO_3$

Saadi Berri[1,2,*] **and Nadir Bouarissa**[2]

[1] *Faculty of Science, University of M'sila, Algeria*

[2] *Laboratory for Developing New Materials and their Characterizations, Setif 1 University-Ferhat ABBAS, Algeria*

Abstract: This study applies first-principles density functional theory calculations to systematically analyze the structural, electronic, and optical behaviors of the $NaTaO_3$ perovskite. Different structures were evaluated for the studied material. The computations were performed using the full-potential linearized augmented plane wave approach together with local orbitals. In order to incorporate exchange–correlation effects, we applied the generalized gradient approximation (GGA) method, which is known to underestimate the bandgap value. To address this limitation, the Tran-Blaha modified Becke–Johnson exchange potential approximation is utilized for enhanced accuracy. The study provides a description of the bulk modulus and pressure derivative of orthorhombic $NaTaO_3$ (*Pbnm*), as well as its density of states and electronic band structure. The structural parameters and stability derived from our calculations are in good agreement with both previous theoretical studies and available experimental data. Electronic structure analysis indicates that the material behaves as a semiconductor, exhibiting direct bandgaps of 3.15 eV using the Tran-Blaha modified Becke–Johnson (TB-mBJ) approach and 2.75 eV within the GGA framework. $NaTaO_3$ exhibits an increase in its bandgap, accompanied by an improvement in physical properties within the TB-mBJ. We present a detailed discussion of the material's optical characteristics. The findings related to its electronic and optical properties indicate strong potential for optoelectronic applications within the visible and ultraviolet spectral ranges.

Keywords: $NaTaO_3$, electronic structure, optical properties, first-principles calculations

1. Introduction

Perovskites, with various compositions and structures, have garnered attention because of their promising uses across diverse industrial and technical fields. They possess many remarkable properties, including their use as mixed-conducting oxides for gas separation [1], spintronics [2], solid oxide fuel cells [3], white light-emitting diodes [4], solar cells [5, 6], photovoltaics (PVs) [7], sensors [8], detectors [9], and thermoelectronics [10].

Technically, direct bandgap semiconductors are solid inorganic materials suitable for optoelectronic devices and related applications [11]. To achieve this, researchers have explored various high-efficiency organic and inorganic materials. Recent advances in solar cells using solid-state materials have demonstrated higher efficiency than previous designs based on thin-film technology [12, 13].

Recently, a wide range of solid materials, including oxides, perovskites, nitrates, spinels, and Heusler materials, have attracted notable interest for their versatile applications [14]. Among these, hybrid perovskites are very important materials in solar cell technology, mainly owing to their outstanding power conversion efficiency (PCE). Extensive scientific research and development have led to remarkable advances in PCE performance, with the latter increasing from 3.8% in 2009 to an impressive 25.6% in 2020 [14].

Several perovskite oxides, including $NaTaO_3$ [15], $KTaO_3$ [16], $BaZrO_3$ [17], $SrTiO_3$ [18], $BaTiO_3$ [19], $CaTiO_3$ [20], $LaFeO_3$ [21], $EuAlO_3$ [22], and $YMnO_3$ [23], exhibit remarkable structural, optical, electrical, and thermal characteristics. Among these, tantalum-based alkali oxides, including $KTaO_3$, $RbTaO_3$, and $CsTaO_3$, exhibit excellent thermal properties and suitable electronic bandgaps, highlighting their potential for photovoltaic and optoelectronic devices [24–37].

Under ultraviolet (UV) irradiation, $NaTaO_3$ (sodium tantalate) is among the most efficient photo-catalysts for water splitting [38, 39] and is also recognized as a promising host material for the development of visible light photo-catalysts [40–43]. $NaTaO_3$ was chosen for this study because it is a stable, layered semiconductor with excellent charge separation capabilities, making it a promising photo-catalyst for H_2 production and other reactions, despite its limitation of being active only under UV light, which is addressed by using co-catalysts or doping to improve performance. Kennedy et al. [44] described atmospheric pressure X-ray diffraction on the $NaTaO_3$ compound, where a structural phase transition was observed. According to the literature, this material undergoes the following phase transition sequence:

$$Pbnm \xrightarrow{720K} Cmcm \xrightarrow{835K} P4/mbm \xrightarrow{893K} Pm\bar{3}m \qquad (1)$$

This work investigates the electronic, structural, and optical properties of $NaTaO_3$ using density functional theory within

---

*Corresponding author:** Saadi Berri, Faculty of Science, University of M'sila and Laboratory for Developing New Materials and their Characterizations, University of Setif 1, Algeria. Email: saadi.berri@univ-msila.dz

TB-mBJ method. We employed the TB-mBJ potential because it yields notably improved bandgap accuracy for semiconductors and insulators without imposing significant computational expense, outperforming standard generalized gradient approximation (GGA) functionals. It provides better accuracy than other multiplicative potentials, making it a valuable tool for understanding and predicting the electronic and optical properties of materials for applications in optoelectronics and spintronics. Our results indicate that $NaTaO_3$ possesses strong potential as a material for optoelectronic devices. The paper is arranged as follows: Section 2 provides an overview of the crystal structure and summarizes the computational techniques and parameters employed. Section 3 discusses the calculated electronic, optical, and structural features of $NaTaO_3$.

2. Computational Details

Our calculations were based on the experimental crystallographic data published by Kennedy et al. [44]. The $NaTaO_3$ compound exhibits crystallization in various symmetries: orthorhombic (space groups *Pbnm* and *Cmcm*), tetragonal (space group *P4/mbm*), and cubic (space group *Pm3m*). Figure 1 provides a depiction of the crystal structure of the $NaTaO_3$ compound. We performed the structural optimization using the GGA [45] implemented through the full-potential linearized augmented plane wave method with local orbitals (FP-LAPW+lo) [46]. This method was implemented to improve the architecture of the WIEN2K code [47] and was used to calculate the total density and range structure for states and the partial density of states. As an exchange-correlation potential, the TB-mBJ method [48] offers a suitable approach for resolving the problem of underestimated bandgaps. The FP-LAPW+lo method was chosen because it was considered the most reliable for considered the most reliable for calculating the electronic band structure [49]. The FP-LAPW+lo method was applied to expand the electric potential and charge density inside Na, Ta, and O atoms using spherical harmonic functions up to *l*max = 10.0. To ensure sufficient convergence, a dense k-point comprising 1000, 3000, and 8000 k-points for the orthorhombic, tetragonal, and cubic phases was used. Calculations were performed until complete charge and energy convergence, with energy accuracy of 10^{-6} Ry and a charge accuracy of 10^{-5} Ry. In this work, the optical properties were evaluated using Brillouin-zone integrations performed over a dense k-point mesh containing 5000 points.

The primary limits of the TB-mBJ method include its inability to be used for total energy calculations because it is not a true density functional, potential failure to accurately treat localized d- or f-states without additional corrections, and the possibility of difficulty achieving self-consistency, sometimes requiring a perturbative approach. Furthermore, while it generally improves bandgaps, it can underestimate gaps for certain classes of solids and may have varying accuracy depending on the specific material or the chosen parameters.

3. Results and Discussion

The initial step involved computing the total energy for each structural configuration as a function of the unit-cell volume. The correlation between the calculated energies and the lattice parameters was then examined and fitted to the Murnaghan E–V equation of state (EOS) [50] to extract the equilibrium values of a(Å), b(Å), c(Å), as well as the bulk modulus B(GPa) and its pressure derivative B'. The structural parameters computed for both phases are summarized in Table 1. The optimal lattice constants a (Å), b (Å), and c (Å) obtained by this procedure are consistent with experimental measurements [44, 51] and available data [52–55]. Figure 2 illustrates the variation of the total energy with respect to unit-cell volume for the different phases. The (*Pbnm*) phase is a

Figure 1
Optimized crystalline structures for $NaTaO_3$

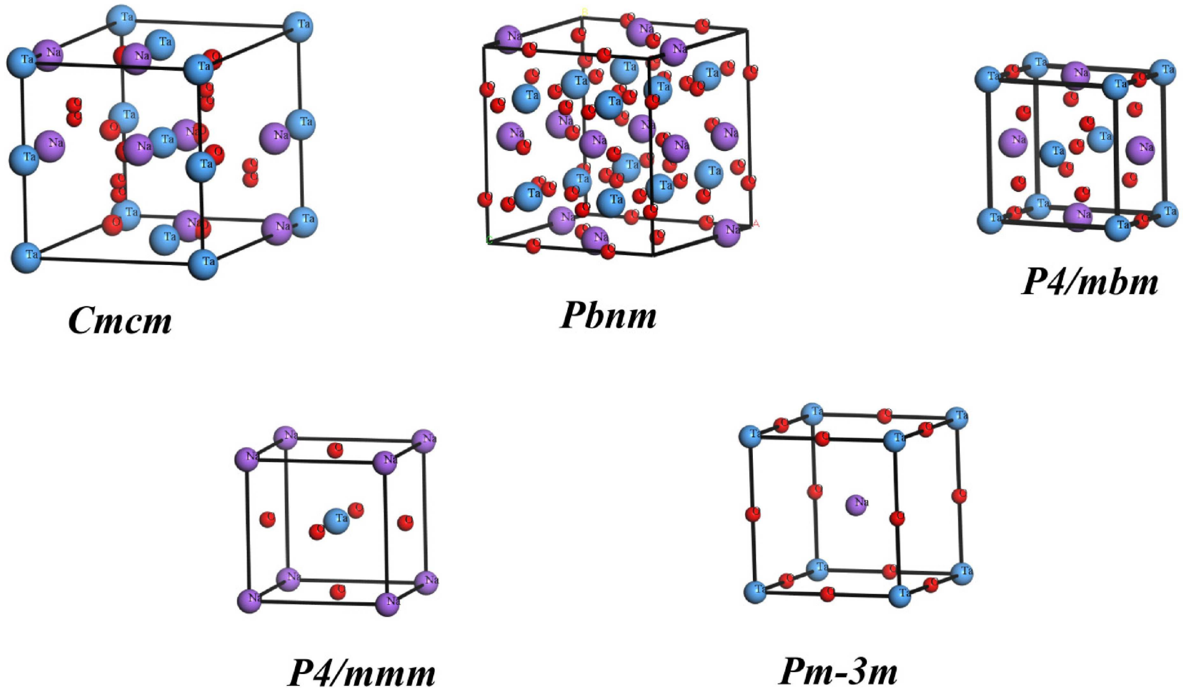

Table 1
Optimized lattice parameters *a* (Å), *b* (Å), *c* (Å), bulk modulus *B* (GPa), and the corresponding pressure derivative *B'* of the $NaTaO_3$ compound

Compound		*a* (Å)	*b* (Å)	*c* (Å)	*B* (GPa)	*B'*
$NaTaO_3$						
Pbnm	This work	5.5915	5.6861	7.9482	197.369	4.2309
	Exp [44]	5.4768	5.5212	7.7890	-	-
Pcmn	Others [52]	5.4992	7.7063	5.3904	-	-
	[53]	5.5335	5.5784	7.7869		
Cmcm	This work	7.9341	7.9982	7.9961	194.495	4.411
	Exp [44]	7.8337	7.8485	7.8552	-	-
P4/mbm	This work	5.5971	-	3.9392	193.326	4.462
	Exp [44]	5.5503	-	3.9335	-	-
	Others[52]	5.4335	-	3.9562		
P4/mmm	This work	3.9821	-	-	192.599	4.468
	Exp [51]	3.9252	-	-	-	-
Pm-3m	This work	3.9822	-	-	192.418	4.649
	Exp [44]	3.9313	-	-	-	-
	Others[53]	3.9462	-	-	-	-
	[54]	3.9475	-	-	204.4481	4.6089
	[55]	3.9858	-	-	191.77	-

Figure 2
The optimization plots computed for $NaTaO_3$

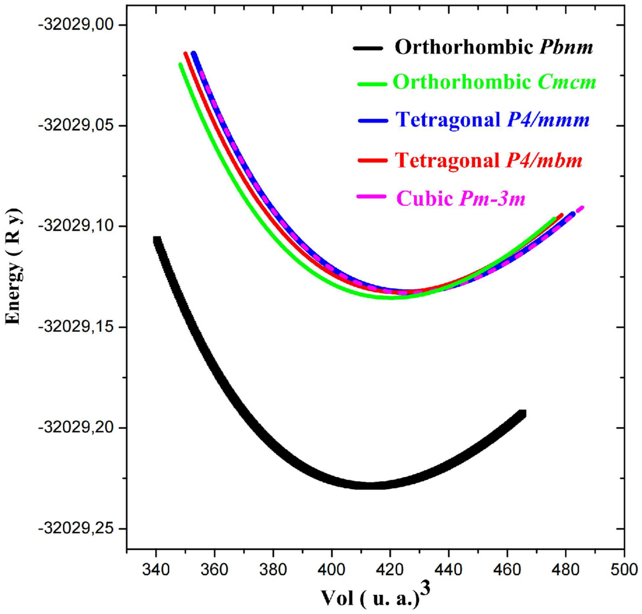

stable ground state for (*Cmcm*), (*P4/mbm*), (*P4/mmm*), and (Pm-3*m*) due to the lowest total energy per unit volume among the five states.

According to X-ray diffraction results by Kennedy et al. [44], $NaTaO_3$ undergoes successive structural transformations: orthorhombic (*Pbnm*) at room temperature, orthorhombic (*Cmcm*) at 720 K, tetragonal (*P4/mbm*) at 835 K, and cubic (*Pm3m*) at temperatures exceeding 893 K. Ismailzde [51] studied the type of $NaTaO_3$, including (*Pbnm*), (*Cmcm*), (*P4/mbm*), and cubic (*Pm-3m*). Under room temperature conditions, $NaTaO_3$ exhibits an orthorhombic distorted perovskite structure with a (*Pbnm*) space group and shows three phase transitions at elevated temperatures, in the sequence (*Pbnm*) 723 K, (*Cmcm*) 833K , and (*P4/mbm)* 893K, (*Pm-3m*). The lattice parameters and the electronic and optical properties of $NaTaO_3$ in the cubic (*Pm-3m*), tetragonal (*P4/mbm*), and orthorhombic (*Pcmn*) phases were also investigated by Ece Eyi and Cabuk [56] using the pseudo-potential plane wave (PP-PW) method within density functional theory. The study focused on calculations of the electronic structure and on optical parameters—dielectric functions, refractive indices, and energy loss as functions of photon energy—for the (Pbnm) phase. This phase was chosen for its stability at room temperature and pressure.

The electronic band structure serves as a fundamental tool for analyzing the electronic and optical behavior of semiconductors [10]. Insight into these parameters is necessary for the design and fabrication of devices based on such semiconductors [13, 14]. Figure 2 shows the resulting band structure, which highlights a distinct energy separation between the VB and CB, called the energy bandgap (Eg). The energy levels in the conduction band allow electrons to move freely, enabling electrical conduction, while the valence band consists of filled electronic states. The gap separating these bands determines the electrical conductivity of the material. For calculations, the Fermi energy (E_F), corresponding to the highest occupied states at absolute zero, is assigned a value of 0 eV, while the effects of finite temperature are neglected. Figures 3 and 4 illustrate the band structures (BS) and total density of states (TDOS) of $NaTaO_3$ in its geometry-optimized orthorhombic structure (*Pbnm*). The TP-mBJ and GGA methods have a general topological similarity. The valence band maximum and the conduction band minimum (CBM) are both found at the Γ point. This characteristic makes the material a promising candidate for photovoltaic applications. Materials with a direct bandgap exhibit higher efficiency than those with an indirect bandgap for optoelectronic applications. This is due to the involvement of

Figure 3
Band structure of $NaTaO_3$ in the (*Pbnm*) structure

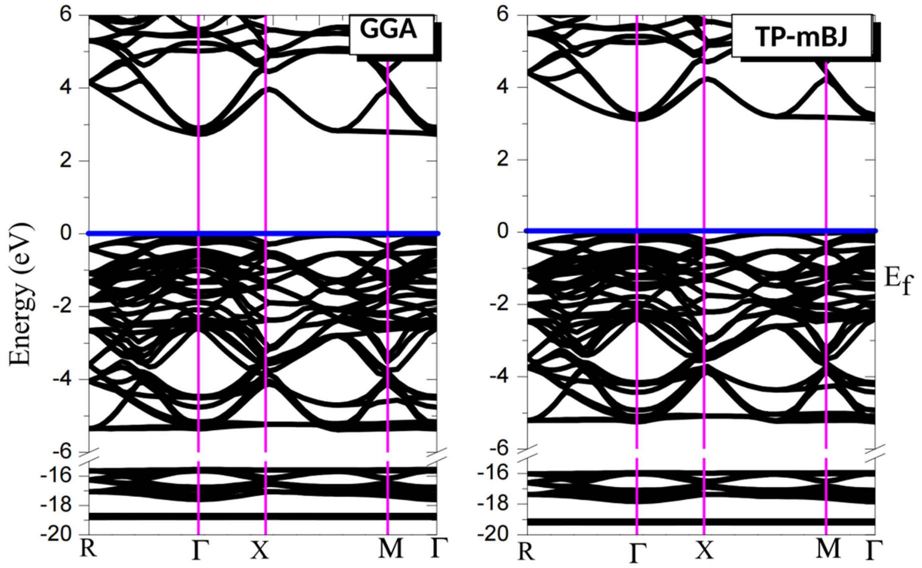

Figure 4
The density of states (DOS), both total and projected, for the (*Pbnm*) structure

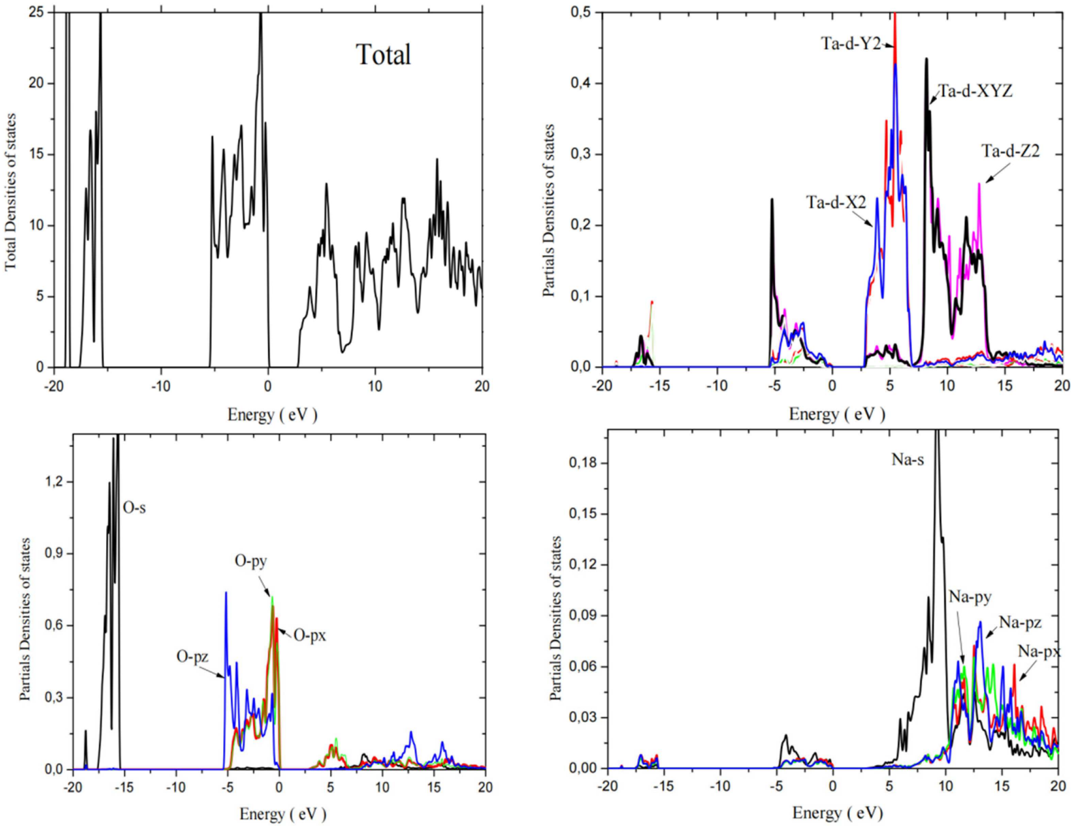

phonons, which makes indirect bandgap semiconductors less efficient light emitters [7, 9]. The energy bandgap determined using GGA is 2.75 eV, while TB-mBJ calculations yield a value of 3.15 eV. The experimentally measured bandgap for $NaTaO_3$ is 3.98 eV [57]. Experimental results suggest that mBJ calculations describe the bandgap of $NaTaO_3$ more accurately than calculations performed with the GGA method. According to Tian et al. [58], electronic structure calculations performed for the (Pbnm) phase using the Vienna Ab initio Simulation Package yielded bandgaps of 2.7 eV (GGA) and 3.92 eV (GGA+U). Wang et al. [59] used a recently developed method to calculate band edge potentials by integrating quasi-particle effects using the GW approximation. It was found in their study that the bandgap of $NaTaO_3$ is 2.89 eV.

The total and partial densities of states (TDOS and PDOS) for $NaTaO_3$ in the (*Pbnm*) phase at equilibrium lattice constants are presented in Figure 4. With the Fermi level positioned at 0 eV, the compound's density of states (DOS) can be broadly classified into three distinct regions. The core electrons mainly contribute from the O-s states at lower energy levels, while the second region, spanning -10 to 0 eV, is largely defined by O-px, O-py, and O-pz states. In the unoccupied states beyond the Fermi level, the d-X2, d-Y2, d-Z2, and d-XYZ orbitals of the sodium atom, hybridized with the Na-s, Na-px, Na-py, and Na-pz states, are significantly represented.

The total and projected DOS of the (*Pbnm*) structure were calculated using the generalized gradient approximation method. Valuable information on the electronic properties is provided in this study, encompassing both the distribution of electronic states across energy levels and the roles of particular atomic orbitals.

The first microscopic dielectric function mainly characterizes the behavior of solid materials under electromagnetic radiation. The material has an orthorhombic crystal structure, the disarrangement of which is specified by the corresponding space group (*Pbnm*). For this type of structure, three components of the dielectric function need to be taken into account [23]. The imaginary part of $\varepsilon(\omega)$ can be expressed as

$$\begin{pmatrix} \mathrm{Im}\varepsilon_{xx} & 0 & 0 \\ 0 & \mathrm{Im}\varepsilon_{yy} & 0 \\ 0 & 0 & \mathrm{Im}\varepsilon_{zz} \end{pmatrix} \quad (2)$$

The real component of the dielectric function indicates how the material responds to an external electric field, considering its polarization. This real component mainly indicates the material's response to polarization, while the imaginary component represents the degree of absorption experienced by the material under external forces. The observed absorption originates from intra-band and inter-band transitions, with intra-band transitions being especially important in metallic systems. Furthermore, inter-band transitions are classified into two categories: direct and indirect. Indirect inter-band transitions involving phonon scattering exert minimal influence on the imaginary component of the dielectric function, and hence these contributions are omitted.

The dielectric function of the studied material exhibits high values in the near-ultraviolet (3.10–4.13 eV) and mid-ultraviolet (4.13–6.20 eV) ranges. In the far-ultraviolet region (6.20–12.4 eV), these values decrease markedly. The imaginary component of the dielectric function reveals that the threshold energies, corresponding to the first critical points, are situated near A1 through A7. These points mainly originate from transitions of electrons between the three VB and five CB levels (see Table 2). This agrees with the excellent photocatalytic performance of $NaTaO_3$ when exposed to ultraviolet light.

The real and imaginary spectra of the dielectric function for $NaTaO_3$, computed by the FP-LAPW method via two distinct approaches, are shown in Figure 5. When the photon energy reaches 4 eV, the real part of the dielectric function increases sharply, but decreases completely around 6 eV. Photons can propagate through the material when the real part is positive. On the other hand, when this part becomes negative, electromagnetic waves undergo damping within the compound. Only longitudinally polarized waves can propagate under the condition that the real part of the dielectric function equals zero. In an orthorhombic structure, the real parts of the dielectric constant gradually approach the static or low-frequency dielectric constants $\varepsilon_1^{xx}(0)$, $\varepsilon_1^{yy}(0)$ and $\varepsilon_1^{zz}(0)$ as the frequency approaches zero.

This can be observed in the Reststrahlen region of the optical spectra. The results for $\varepsilon_1^{xx}(0)$, $\varepsilon_1^{yy}(0)$, and $\varepsilon_1^{zz}(0)$ under applied load, using both GGA and TB-mBJ methods, are presented in Table 3. These values enabled the determination of the material's energy bandgap using the Penn model, i.e., $\varepsilon_1(0)1+(\hbar w_p/E_g)^2$ [60]. It is well known that $\varepsilon_1(0)$ is inversely related to the fundamental energy bandgap; hence, a smaller $\varepsilon_1(0)$ reflects a larger bandgap.

This function serves as a key descriptor of the energy dissipation mechanisms due to electron excitations and inter-band transitions within the material. The study of $L(\omega)$ provides valuable information on the optical properties, electronic interactions, and plasmonic behavior in the stable lattice configuration of the material.

The refractive index $n(\omega)$ and energy loss $L(\omega)$ spectra of $NaTaO_3$ are presented in Figures 6 and 7, respectively, and were calculated using the two approaches studied in this work. Figure 6 reveals that the material exhibits pronounced quenching effects near the ultraviolet. With increasing photon energy, these effects become less pronounced. The energy loss of high-velocity electrons moving through the material is shown in Figure 7. From the analysis, two distinct peaks appear at photon energies of 7.70 eV and 7.65 eV, determined by the GGA and TB-mBJ methods. The peaks in Figure 7 correspond to the plasma resonance, denoted by the frequency ωp. This frequency, called the volume plasma frequency, is defined by the conditions $\varepsilon_1(\omega) = 0$ and $\varepsilon_2(\omega) < 1$ [61, 62]. To identify the peaks corresponding to the plasma resonance (ωp) in Figure 7, the authors would typically analyze the spectral response (e.g., reflectance, scattering, or absorption) where significant changes in a metal-based plasmonic system occur. The plasma resonance frequency (ωp) is a fundamental property of the material itself, representing the collective oscillation of free electrons, and it manifests as a distinct peak or

Table 2
Determination of the key peak locations in the imaginary dielectric function of $NaTaO_3$

	A1	A2	A3	A4
GGA	2.97	3.64	4.28	5.17
TP-mBJ	3.27	3.91	4.51	5.08
Transitions	O-px→Ta-d-X2	O-px→Ta-d-Y2	O-px→Na-s	O-py→Ta- d-XYZ
	A5	A6	A7	
GGA	6.04	6.23	7.08	
TP-mBJ	5.57	6.00	6.74	
Transitions	O-py→Ta-d-Z2	O-pz→Ta-d-XYZ	O-pz→Ta-d-Z2	

Figure 5
Investigation of the real ($\varepsilon_1(\omega)$) and imaginary ($\varepsilon_2(\omega)$) components of the dielectric function $\varepsilon(\omega)$ for $NaTaO_3$ in its (*Pbnm*) crystal structure at equilibrium lattice constant

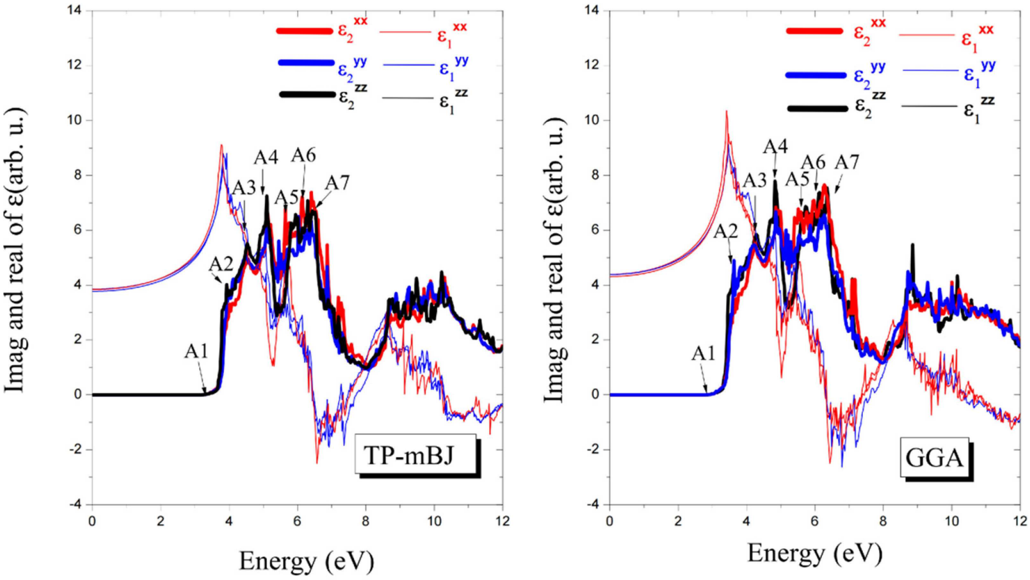

Table 3
Determination of static constants and energy bandgap for the structure (*Pbnm*)

	$E_g(eV)$	$\varepsilon_1^{xx}(0)$	$\varepsilon_1^{yy}(0)$	$\varepsilon_1^{zz}(0)$	$n^{xx}(0)$	$n^{/yy}(0)$	$n^{zz}(0)$
GGA	1.86	4.28	4.38	4.41	2.07	2.09	2.10
TB-mBJ	3.15	3.75	3.84	3.86	1.94	1.95	1.96

Figure 6
The refractive index n(ω) of the $NaTaO_3$ perovskite compound in the (*Pbnm*) structure at the equilibrium lattice constants

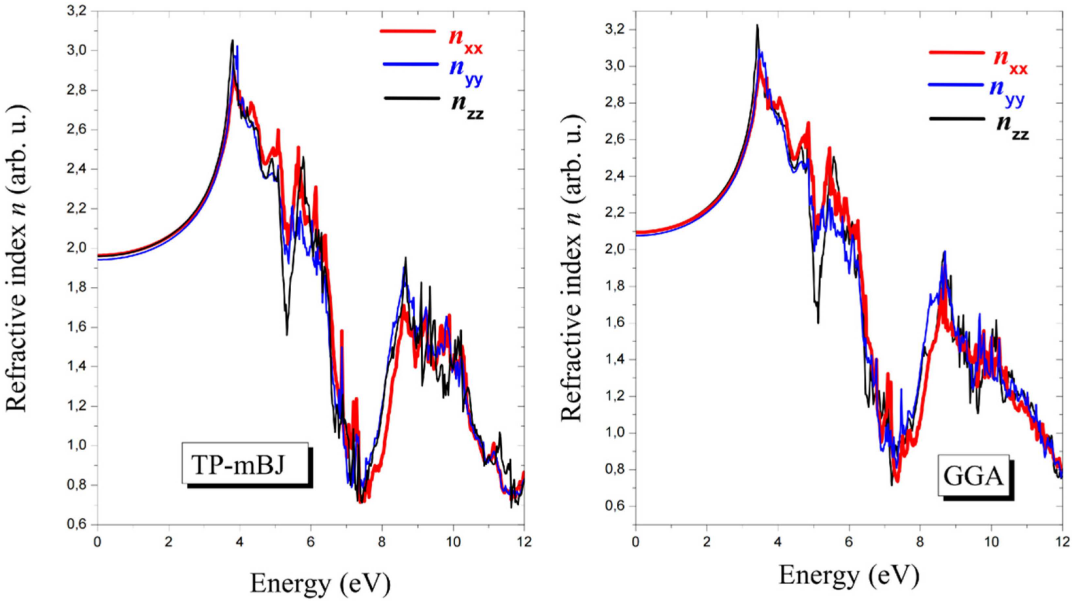

Figure 7
The energy loss function *L(ω)* for the perovskite compound $NaTaO_3$, crystallized in the (*Pbnm*) structure, is evaluated at its equilibrium lattice constant

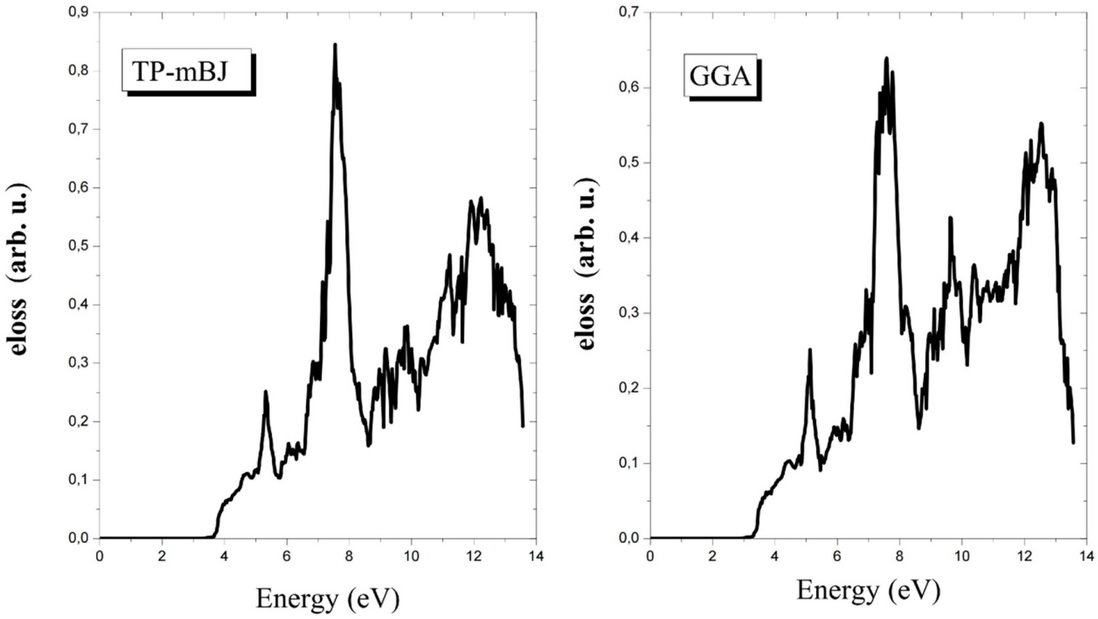

dip in the experimental spectrum at that specific frequency. This sharp decline in reflectance implies that, according to the GGA and TB-mBJ calculations, the material becomes transparent for incident photons with energies above 7.70 eV and 7.65 eV, respectively. Therefore, the $NaTaO_3$ compound has potential for application in devices such as Bragg reflectors, as well as in various optical and optoelectronic systems.

It should be noted that the strain in $NaTaO_3$ thin films induces structural changes, modifying the bandgap and electronic properties, which can lead to enhanced photo-catalytic performance by improving bandgap alignment and charge carrier mobility, and potentially inducing metallic or magnetic states in ultrathin films.

4. Conclusions

The full-potential linearized augmented plane wave plus local orbitals (FP-LAPW+lo) method implemented in the Wien2k code was employed to investigate the structural, electronic, and optical properties of $NaTaO_3$ within both GGA and TB-mBJ approaches. Key parameters, including the lattice constant, bulk modulus, and its pressure derivative, are reported. The theoretically predicted lattice parameters for $NaTaO_3$ in the orthorhombic (*Pbnm and Cmcm*), tetragonal (*P4/mbm* and *P4/mmm*), and cubic (*Pm-3m*) phases are in good agreement with available experimental measurements. This material exhibits direct energy bandgaps ($\Gamma \rightarrow \Gamma$) of approximately 3.15 eV with TB-mBJ and 2.75 eV with GGA. Furthermore, its optical properties were calculated and analyzed in detail. Essential optical parameters, including the dielectric function, refractive index, and energy loss, were evaluated and examined in detail.

Ethical Statement

This study does not contain any studies with human or animal subjects performed by any of the authors.

Conflicts of Interest

The authors declare that they have no conflicts of interest to this work.

Data Availability Statement

Data are available from the corresponding author upon reasonable request.

Author Contribution Statement

Saadi Berri: Conceptualization, Methodology, Software, Validation, Formal analysis, Investigation, Writing - original draft, Writing - review & editing, Visualization, Supervision, Project administration. **Nadir Bouarissa:** Validation, Formal analysis, Writing - review & editing.

References

[1] Pan, Z., Huang, H., Wang, Y., Wang, T., Yu, H., Ma, Q., . . . , & Yang, Y. (2025). Novel metal oxides partially derived perovskite-structured hydroxides for room temperature trace NO_2 gas sensors under UV irradiation. *Talanta*, *286*, 127449. https://doi.org/10.1016/j.talanta.2024.127449

[2] Haque, M. A., & Beard, M. C. (2025). Spin effects in metal halide perovskite semiconductors. *Nanoscale*, *17*(16), 9895–9906. https://doi.org/10.1039/D5NR00127G

[3] Yao, C., Xia, B., Zhang, H., Wang, H., Zhang, W., Guo, Q., . . . , & Cai, K. (2025). Fluoride-driven modulation of oxygen vacancies and surface stability in cobalt-based perovskite as a high-performance cathode for solid oxide fuel cells. *Chemical Engineering Journal*, *505*, 159359. https://doi.org/10.1016/j.cej.2025.159359

[4] Shen, C., Fang, S., Zhang, J., Liang, X., Su, C., Qing, J., . . . , & Hou, L. (2024). High performance and stable pure-blue

quasi-2D perovskite light-emitting diodes by multifunctional zwitterionic passivation engineering. *Advanced Photonics*, *6*(2), 026002–026002. https://doi.org/10.1117/1.AP.6.2.026002

[5] Seyisi, T., Fouda-Mbanga, B. G., Mnyango, J. I., Nthwane, Y. B., Nyoni, B., Mhlanga, S., . . . , & Tywabi-Ngeva, Z. (2025). Major challenges for commercialization of perovskite solar cells: A critical review. *Energy Reports*, *13*, 1400–1415. https://doi.org/10.1016/j.egyr.2025.01.019

[6] Suo, J., Yang, B., Bogachuk, D., Boschloo, G., & Hagfeldt, A. (2025). The dual use of SAM molecules for efficient and stable perovskite solar cells. *Advanced Energy Materials*, *15*(2), 2400205. https://doi.org/10.1002/aenm.202400205

[7] Shrivastav, N., Madan, J., Mohammed, M. K. A., Al-Mousoi, A. K., Hossain, M. K., Amami, M., ..., & Pandey, R. (2023). Optimizing the performance of $Cs_2AgBiBr_6$ based solar cell through modification of electron and hole transport layers. *Materials Today Communications*, *36*, 106761. https://doi.org/10.1016/j.mtcomm.2023.106761

[8] Bui, T. H., & Shin, J. H. (2023). Perovskite materials for sensing applications: Recent advances and challenges. *Microchemical Journal*, *191*, 108924. https://doi.org/10.1016/j.microc.2023.108924

[9] Li, H., Li, J., Shen, N., Chen, S., Wei, H., & Xu, B. (2024). Progress and challenges of metal halide perovskites in X-ray detection and imaging. *Nano Energy*, *119*, 109055. https://doi.org/10.1016/j.nanoen.2023.109055

[10] Berri, S. (2022). Thermoelectric properties of A_2BCl_6: A first principles study. *Journal of Physics and Chemistry of Solids*, *170*, 110940. https://doi.org/10.1016/j.jpcs.2022.110940

[11] Dong, H., Ran, C., Gao, W., Li, M., Xia, Y., & Huang, W. (2023). Metal Halide Perovskite for next-generation optoelectronics: Progresses and prospects. *eLight*, *3*(1), 3. https://doi.org/10.1186/s43593-022-00033-z

[12] van Truong, D., Quang, T. T., Linh, N. H., van, Hoi., N, & van Thanh, V. (2020). Strain effect on hysteresis loop of $PbTiO_3$ bulk. In *Advances in Engineering Research and Application: Proceedings of the International Conference on Engineering Research and Applications*, 679–685. https://doi.org/10.1007/978-3-030-37497-6_78

[13] van Truong, D., Quang, T. T., Linh, N. H., van, Hoi., N, & van Thanh, V. (2023). Enhancement of polarization properties of bulk $PbTiO_3$ by engineering strain. *Integrated Ferroelectrics*, *232*(1), 186–196. https://doi.org/10.1080/10584587.2023.2173453

[14] Ahmedbowba, S., Khadri, F., Ouerghui, W., & Ridene, S. (2025). Study of the structural and electronic properties of $Zn_{1-x-y}Mg_xTi_yO$ structures. *Journal of Vacuum Science & Technology B*, *43*(4), 042211. https://doi.org/10.1116/6.0004706

[15] Fresno, F., Jana, P., Reñones, P., Coronado, J. M., Serrano, D. P., & de la Peña O'Shea, V. A. (2017). CO_2 reduction over $NaNbO_3$ and $NaTaO_3$ perovskite photocatalysts. *Photochemical & Photobiological Sciences*, *16*(1), 17–23. https://doi.org/10.1039/c6pp00235h

[16] Modak, B., & Ghosh, S. K. (2017). Improving visible light photocatalytic activity of $KTaO_3$ using cation-anion dopant pair. *Solar Energy Materials and Solar Cells*, *159*, 590–598. https://doi.org/10.1016/j.solmat.2016.10.003

[17] Datta, A. K., Hossain, M. K., Revathy, M. S., Reddy, M. S., Singh, A., Radhika, S., ..., & Haldhar, R. (2025). A first principle investigation to explore the effect of Zr-site Ti doping on structural, electronic, optical, and mechanical properties of $BaZrO_3$. *Scientific Reports*, *15*(1), 26380. https://doi.org/10.1038/s41598-025-11576-9

[18] Zhuang, J., Wang, J., & Yan, F. (2023). Review on chemical stability of lead halide perovskite solar cells. *Nano-Micro Letters*, *15*(1), 84. https://doi.org/10.1007/s40820-023-01046-0

[19] Kanwal, S., Badawi, A. K., Khan, A. M., Khan, R. A., Shahzad, W., & Ismail, B. (2025). Assessment of thermodynamic properties of $SrSnO_3$ perovskite for enhanced photocatalytic applications. *Journal of Inorganic and Organometallic Polymers and Materials*, *35*(7), 5767–5789. https://doi.org/10.1007/s10904-025-03621-x

[20] Bouzaid, A., Ziat, Y., Belkhanchi, H., & Fatihi, H. (2025). Boosting the photocatalytic hydrogen production via the S/Zr co-doping in a $CaTiO_3$ perovskite: First-principles study of the optoelectronic, thermodynamic, and photocatalytic. *The European Physical Journal B*, *98*(7), 160. https://doi.org/10.1140/epjb/s10051-025-01004-2

[21] Nair, R., Uppuluri, K., Paul, F., Sirengo, K., Szwagierczak, D., Pillai, S. C., & Manjakkal, L. (2025). Electrochemical energy storing performances of printed $LaFeO_3$ coated with PEDOT:PSS for hybrid supercapacitors. *Chemical Engineering Journal*, *504*, 158781. https://doi.org/10.1016/j.cej.2024.158781

[22] Zhao, J., Wang, X., Li, H., & Xu, X. (2024). Interpretable machine learning-assisted screening of perovskite oxides. *RSC Advances*, *14*(6), 3909–3922. https://doi.org/10.1039/D3RA08591K

[23] Wan, F., Hua, X., & Guo, Q. (2024). Modulation of the structural, magnetic, and dielectric properties of $YMnO_3$ by cu doping. *Materials*, *17*(12), 2929. https://doi.org/10.3390/ma17122929

[24] Kumar, S., Tiwari, S. C., Gupta, A., Verma, A., & Kumar, A. (2025). Comprehensive study of $BaAlO_3$ using FP-LMTO and PBE-GGA: Structural, electronic, and optical properties. *Semiconductors*, *59*(5), 495–501. https://doi.org/10.1134/S1063782625600329

[25] Nguyen, H. L., The Quang, T., Nguyen, M. S., Thang, T., van Thanh, V., & van Truong, D. (2023). Theoretical computational of electronic and transport properties and optical conductivity of monolayer NiS2 under mechanical strain. *JST Engineering and Technology for Sustainable Development*, *33*(1), 34–41. https://doi.org/10.51316/jst.164.etsd.2023.33.1.5

[26] Kumar, A., Kumar, A., & Iram, N. (2024). First-principles calculations to investigate structural, electronic, mechanical and optical properties of $SrAlO_3$ compound. *Hybrid Advances*, *6*, 100211. https://doi.org/10.1016/j.hybadv.2024.100211

[27] Kumar, A., Pandey, N., Punetha, D., Saha, R., & Chakrabarti, S. (2023). Enhancement in the structural and optical properties after incorporation of reduced graphene oxide (rGO) nanocomposite in pristine $CsSnBr_3$ for solar cell application. *ACS Applied Electronic Materials*, *5*(6), 3144–3153. https://doi.org/10.1021/acsaelm.3c00224

[28] Mustafa, G. M., Farooq, M. U., Ameer, M. A., Noor, N. A., Saeed, Y., Mumtaz, S., & Elhindi, K. M. (2025). Investigations of mechanical, magnetic and thermoelectric properties of double perovskites Na_2IrX_6 (X=Cl, Br) for spintronic and energy harvesting applications. *Materials Chemistry and Physics*, *334*, 130501. https://doi.org/10.1016/j.matchemphys.2025.130501

[29] Viswanath, N. S. M., & Im, W. B. (2025). Underlying dynamics of double-halide perovskites: Unraveling structural complexity, bandgap modulation, optical, and carrier dynamics for next-generation optoelectronics. *ACS Applied*

Optical Materials, *3*(3), 578–600. https://doi.org/10.1021/acsaom.4c00524

[30] Ghani, M. U., Junaid, M., Batoo, K. M., Ijaz, M. F., & Zazoum, B. (2025). An extensive study of structural, electronic, optical, mechanical, and thermodynamic properties of inorganic oxide perovskite materials $ScXO_3$ (X = Ga, In) for optoelectronic applications: A DFT study. *Inorganic Chemistry Communications*, *172*, 113459. https://doi.org/10.1016/j.inoche.2024.113459

[31] Rached, H., Rached, D., Caid, M., Amrani, L., Rached, Y., Mansour, H., ..., & Belkacem, A. A. A. (2025). Future insights into double perovskites Ba_2AlTMO_6 (TM = W, Re, and Os) for sustainable and clean energy production: A DFT investigation using GGA, TB-mBJ, and HSE06 methods. *Journal of Inorganic and Organometallic Polymers and Materials*, *35*(7), 5239–5260. https://doi.org/10.1007/s10904-024-03584-5

[32] Berri, S. (2020). Theoretical analysis of the structural, electronic, optical and thermodynamic properties of trigonal and hexagonal $Cs_3Sb_2I_9$ compound. *The European Physical Journal B*, *93*(10), 191. https://doi.org/10.1140/epjb/e2020-10143-1

[33] Berri, S. (2017). Theoretical analysis of the structural, electronic and optical properties of tetragonal Sr_2GaSbO_6. *Chinese Journal of Physics*, *55*(6), 2476–2483. https://doi.org/10.1016/j.cjph.2017.11.001

[34] Berri, S. (2025). Evaluating hydrogen storage potential of Cs_2ABH_6: DFT-based approach. *Modern Electronic Materials*, *11*(1), 19–30. https://doi.org/10.3897/j.moem.11.1.136072

[35] Mushtaq, I., Ahmed, A., Ahmad, M., Lien, J.-C., Zhang, T.-W., Aiman, U., & Hussain, M. (2025). Exploring the nonlinear optical properties of difluorobenzyl derivatives: Synthesis and DFT analysis. *Structural Chemistry. Advance online publication*. https://doi.org/10.1007/s11224-025-02554-y

[36] Lachenani, H., Ouir, S., Boudeffar, F., Achacha, S., Menari, H., Krea, M., & Gabouze, N. (2024). Study of optical properties of porous silicon by DFT, comparison to experimental and effective medium approximation methods. *Bulletin of Materials Science*, *47*(3), 128. https://doi.org/10.1007/s12034-024-03189-1

[37] Berri, S. (2022). First principle analysis of structural, electronic, optical, and thermoelectric characteristics of $Ba_3CaTa_2O_9$ complex perovskite. *Emergent Materials*, *5*(6), 1849–1857. https://doi.org/10.1007/s42247-021-00331-1

[38] Lee, Y.-C., Teng, H., Hu, C.-C., & Hu, S.-Y. (2008). Temperature-dependent photoluminescence in $NaTaO_3$ with different crystalline structures. *Electrochemical and Solid-State Letters*, *11*(2), P1–P4. https://doi.org/10.1149/1.2817476

[39] Kato, H., Asakura, K., & Kudo, A. (2003). Highly efficient water splitting into H_2 and O_2 over lanthanum-doped $NaTaO_3$ photocatalysts with high crystallinity and surface nanostructure. *Journal of the American Chemical Society*, *125*(10), 3082–3089. https://doi.org/10.1021/ja027751g

[40] Kanhere, P., Zheng, J., & Chen, Z. (2012). Visible light driven photocatalytic hydrogen evolution and photophysical properties of Bi^{3+} doped $NaTaO_3$. *International Journal of Hydrogen Energy*, *37*(6), 4889–4896. https://doi.org/10.1016/j.ijhydene.2011.12.056

[41] Kang, H. W., Lim, S. N., & Park, S. B. (2012). Photocatalytic H_2 evolution under visible light from aqueous methanol solution on $NaBi_xTa_{1-x}O_3$ prepared by spray pyrolysis. *International Journal of Hydrogen Energy*, *37*(5), 4026–4035. https://doi.org/10.1016/j.ijhydene.2011.12.006

[42] Yang, M., Huang, X., Yan, S., Li, Z., Yu, T., & Zou, Z. (2010). Improved hydrogen evolution activities under visible light irradiation over $NaTaO_3$ codoped with lanthanum and chromium. *Materials Chemistry and Physics*, *121*(3), 506–510. https://doi.org/10.1016/j.matchemphys.2010.02.015

[43] Yi, Z. G., & Ye, J. H. (2007). Band gap tuning of $Na_{1-x}LaxTa_{1-x}Co_xO_3$ solid solutions for visible light photocatalysis. *Applied Physics Letters*, *91*(25), 254108. https://doi.org/10.1063/1.2826277

[44] Kennedy, B. J., Prodjosantoso, A. K., & Howard, C. J. (1999). Powder neutron diffraction study of the high temperature phase transitions in $NaTaO_3$. *Journal of Physics: Condensed Matter*, *11*(33), 6319–6327. https://doi.org/10.1088/0953-8984/11/33/302

[45] Perdew, J. P., Burke, K., & Ernzerhof, M. (1996). Generalized gradient approximation made simple. *Physical Review Letters*, *77*(18), 3865–3868. https://doi.org/10.1103/PhysRevLett.77.3865

[46] Blaha, P., Schwarz, K., Medsen, G. K. H., Kvasnicka, D., & Luitz, J. (2001). *WIEN2k: An augmented plane wave plus local orbitals program for calculating crystal properties*. Vienna University of Technology.

[47] Blaha, P., Schwarz, K., Sorantin, P., & Trickey, S. B. (1990). Full-potential, linearized augmented plane wave programs for crystalline systems. *Computer Physics Communications*, *59*(2), 399–415. https://doi.org/10.1016/0010-4655(90)90187-6

[48] Engel, E., & Vosko, S. H. (1993). Exact exchange-only potentials and the virial relation as microscopic criteria for generalized gradient approximations. *Physical Review B*, *47*(20), 13164–13174. https://doi.org/10.1103/PhysRevB.47.13164

[49] Rahman, A., Haneef, M., Alrebdi, T. A., & Amin, B. (2025). Exploring the Physical Properties of Indium Based Halide Double Perovskites for Optoelectronic and Photocatalytic Applications: A DFT Study. *Computational Condensed Matter*, *45*, e01167. https://doi.org/10.1016/j.cocom.2025.e01167

[50] Murnaghan, F. D. (1944). The compressibility of media under extreme pressures. *Proceedings of the National Academy of Sciences*, *30*(9), 244–247. https://doi.org/10.1073/pnas.30.9.244

[51] Ismailzade, I. G. (1963). An X-ray diffraction study of phase transitions in sodium tantalate. *Soviet Physics. Crystallography*, *7*(5), 584-587.

[52] Ismael, S. M. H., Hashim, N. S., Al-Saymari, F. A., Sultan, H. A., Hassan, Q. M. A., Hussein, K. A., ..., & Jarallah, H. M. (2025). Synthesize of an azo compound: Investigation its optical nonlinear properties and DFT study. *Journal of Fluorescence*, *35*(8), 7241–7260. https://doi.org/10.1007/s10895-024-04082-0

[53] Kanhere, P., Shenai, P., Chakraborty, S., Ahuja, R., Zheng, J., & Chen, Z. (2014). Mono- and co-doped $NaTaO_3$ for visible light photocatalysis. *Physical Chemistry Chemical Physics*, *16*(30), 16085–16094. https://doi.org/10.1039/C4CP01000K

[54] Bouafia, H., Hiadsi, S., Abidri, B., Akriche, A., Ghalouci, L., & Sahli, B. (2013). Structural, elastic, electronic and thermodynamic properties of $KTaO_3$ and $NaTaO_3$: Ab initio investigations. *Computational Materials Science*, *75*, 1–8. https://doi.org/10.1016/j.commatsci.2013.03.030

[55] Zhao, N., Wang, Y.-H., Wang, Q.-X., & Hu, W.-J. (2012). First-principles calculations of the electronic structure and optical properties of $K_{1-x}Na_xTaO_3$ (x=0, 0.25, 0.5, 0.75, 1). *Journal of Solid State Chemistry*, *194*, 37–42. https://doi.org/10.1016/j.jssc.2012.07.041

[56] Ece Eyi, E., & Cabuk, S. (2010). Ab initio study of the structural, electronic and optical properties of $NaTaO_3$. *Philosophical Magazine*, *90*(21), 2965–2976. https://doi.org/10.1080/14786431003752159

[57] Liu, D.-R., Wei, C.-D., Xue, B., Zhang, X.-G., & Jiang, Y.-S. (2010). Synthesis and photocatalytic activity of N-doped $NaTaO_3$ compounds calcined at low temperature. *Journal of Hazardous Materials*, *182*(1–3), 50–54. https://doi.org/10.1016/j.jhazmat.2010.05.136

[58] Tian, P.-L., Jiang, Z.-Y., Zhang, X.-D., Zhou, B., Dong, Y.-R., & Liu, R. (2017). Visible light absorption of (Fe, C/N) co-doped $NaTaO_3$: DFT+U. *Chinese Physics B*, *26*(8), 087102.

[59] Wang, H., Wu, F., & Jiang, H. (2011). Electronic band structures of $ATaO_3$ (A = Li, Na, and K) from first-principles many-body perturbation theory. *The Journal of Physical Chemistry C*, *115*(32), 16180–16186. https://doi.org/10.1021/jp2047294

[60] Penn, D. R. (1962). Wave-number-dependent dielectric function of semiconductors. *Physical Review*, *128*(5), 2093–2097. https://doi.org/10.1103/PhysRev.128.2093

[61] Hadi, H. M. (2025). DFT study of electronic and optical properties of pentacene derivatives. *Journal of Molecular Modeling*, *31*(4), 115. https://doi.org/10.1007/s00894-025-06347-2

[62] Darugar, V., Vakili, M., Heydari, S., & Berenji, A. R. (2024). Conductance characteristics of naphthopyran as a light-sensitive molecular optical junction: A joint NEGF-DFT and TD-DFT study. *Journal of Computational Electronics*, *23*(6), 1306–1314. https://doi.org/10.1007/s10825-024-02215-z

How to Cite: Berri, S., & Bouarissa, N. (2025). First-Principles Study of the Structural, Electronic, and Optical Properties of $NaTaO_3$. *Journal of Optics and Photonics Research*. https://doi.org/10.47852/bonviewJOPR52027104